Threshold behavior in quantum-dot nanolasers: Effects of inhomogeneous broadening

Giampaolo D'Alessandro [1], Gian Luca Lippi [2] and Francesco Papoff [3,*]

[1] *School of Mathematical Sciences, University of Southampton, Southampton SO17 1BJ, England, United Kingdom*

[2] *Université Côte d'Azur, UMR 7710 Centre National de la Recherche Scientifique, Institut de Physique de Nice, 17 rue Julien Lauprêtre, 06200 Nice, France*

[3] *Department of Physics, University of Strathclyde, 107 Rottenrow, Glasgow G4 0NG, Scotland, United Kingdom*

(Received 14 July 2025; accepted 10 November 2025; published 11 December 2025)

We investigate the threshold behavior of lasers under various modeling approaches, considering different numbers of nonlasing cavity modes and analyzing the effects of radiation-matter coupling strength, cavity lifetime, and quantum-dot properties. Thermal and electron-electron decoherence are incorporated as phenomenological relaxation processes, in line with established practices. Both spectrally uniform and polydisperse quantum dots are examined. For the former, we observe strong agreement across modeling approaches: the qualitative behavior remains consistent, with threshold pump values showing quantitative shifts depending on the specific model. In the case of polydisperse quantum dots, leading to inhomogeneous broadening, this picture is reaffirmed—each model type exhibits similar qualitative trends, while threshold variations arise due to the stochastic distribution of emitter transition frequencies. Our results confirm that models that assume homogeneous quantum dots are suitable for comparison with experimental data and that inhomogeneous effects can be directly captured using our framework when required.

DOI: 10.1103/m9px-p28x

I. INTRODUCTION

Quantum dots (QDs) have typical sizes of tens of nanometers and function as artificial atoms with discrete, tunable emission; for these reasons, they have emerged as highly promising active media for laser emission, particularly at the micro- and nanoscale. Their discrete energy levels, stemming from strong carrier confinement [1], result in narrow linewidths and reduced carrier-induced refractive index modulation. This yields a lower α factor in the small gain regime [2], typically an order of magnitude smaller than that in quantum wells, enhancing stability and reducing sensitivity to optical feedback [3].

QDs exhibit broadband absorption under optical pumping and are easily excited electrically via the wetting layer of the underlying quantum well. The absorbed energy is efficiently funneled into narrow transitions between discrete levels, enabling high conversion efficiency, ultralow lasing thresholds, and reduced thermal load [4], crucial in the context of data center energy demands [5,6]. Efficient electron-photon coupling and minimized nonradiative recombination—especially with surface passivation [7,8]—further boost efficiency.

Strong electron localization in QDs reduces carrier diffusion and recombination losses, contributing to lower excitation thresholds [9]. Their energy levels exhibit reduced sensitivity to temperature variations compared to bulk or quantum-well structures [10,11], offering improved (albeit modest) temperature stability [12,13]. The emission wavelength is tunable via QD size [14–16], facilitating coupling to resonant cavities [17]—a key requirement for efficient nanoscale laser operation.

QDs tunable emission makes them ideal for lab-on-a-chip applications and integrated photonics [18]. Their subwavelength size and compatibility with solid-state platforms make them excellent candidates for miniaturized devices. Additionally, their ability to support precise gain and loss control is advantageous for emerging non-Hermitian photonics applications, including parity-time symmetric lasers and enhanced sensing [19–23].

Despite these benefits, QDs face limitations due to size dispersion, which leads to inhomogeneous broadening and spectral variability [14–16]. Even minor size variations cause significant wavelength spread [24], affecting exciton and biexciton energy distributions [25] and inducing dephasing [26], ultimately degrading phenomena like superradiance [27]. This broadening reduces the number of QDs effectively participating in lasing [9,28].

Inhomogeneity stems from various factors: confinement dependence on size and shape [29,30], composition and doping [31], surface states [24], and fabrication techniques [32], including colloidal methods [33].

Early QD lasers were dominated by inhomogeneous broadening [34], prompting modeling efforts [35,36] and manufacturing improvements [37]. Advances include efforts to improve array uniformity [38], and morphology and site control [39–41], even for quantum information applications [42]. Recent techniques such as substrate patterning [43], site strain engineering [44], self-alignment [45], nucleation layer [46], and machine learning [47] have significantly improved

*Contact author: f.papoff@strath.ac.uk

QD uniformity. Notably, the frequency distribution of QDs has been quantitatively assessed [48], providing benchmarks for current fabrication capabilities.

To mitigate inhomogeneities, strategies such as optical cavity filtering [18] and thermal tuning [49] have been applied, though these can broaden the emission spectrum [50], reduce gain efficiency [9], and increase cavity losses and threshold currents [51].

Theoretical advances have paralleled fabrication improvements. First-principles models incorporating surface defects, confinement, and environmental interactions [52,53] have informed design. Quantum nanolaser models based on Heisenberg-Langevin equations [54], density matrix theory [55], nonequilibrium Green's functions [56], and cluster expansion [57] often neglect fast, coherent dynamics to focus on slower quantum correlations [58–61].

More recently, semiclassical models like the coherent-incoherent model (CIM) [62,63] have reintroduced coherent field and polarization dynamics while omitting rapidly varying correlations. The CIM captures threshold behavior, observable via first-order coherence functions $g^{(1)}(\tau)$ [64], where coherent emission emerges continuously beyond threshold [65], echoing macroscopic laser theory.

However, fully quantum treatments like the two-particle model (TPM) [66] reveal markedly different behavior: coherent and incoherent emissions become bistable, and the coherent emission at threshold is finite rather than vanishing.

Interpreting these results requires addressing two unresolved issues in CIM and TPM. First, how the lasing threshold depends on pump rate and cavity decay rate—two experimentally tunable parameters—needs clarification. Second, the impact of QD inhomogeneity remains critical. Despite technical progress, variations in QD size and emission frequency persist [59], influencing threshold behavior, coherence, and frequency stability. These effects are particularly significant for quantum models sensitive to coherence loss [17,27], and must be reevaluated in the context of newer frameworks incorporating both coherent and incoherent quantum fields [62,65,67].

In the next section we first extend the CIM and TPM introduced in Refs. [62,65,67] to include the effect of polydisperse QDs. We then introduce a reduced model, the $\mathrm{TPM_{1F}}$, that is ideally suited for the analysis of polydisperse QD models when electron-electron correlations are negligible. In Sec. III we analyze in detail the threshold behavior in the computationally easier case of monodisperse QDs. We relax this condition in Sec. IV where we show that having different QDs does not qualitatively change the threshold behavior. A summary of this work and an exposition of its experimental and engineering consequences conclude the paper. The numerical methodology followed to integrate and analyze the models is summarized in Appendix A. All the equations are listed in the Appendixes, which contain also additional graphs and a justification of the parameter values used in the simulations.

II. COHERENT-INCOHERENT MODELS

We focus on nanolasers in which each QD possesses two localized energy levels, with electrons and holes injected into these levels from the wetting layer. We consider light-matter interaction in the weak-coupling regime, and QDs operating at cryogenic temperatures [60]. Coulomb [58,61] and phonon [68] scattering processes are included, as is customary, via dephasing terms, thus offering a glimpse into the predictions for higher-temperature operation; the interaction Hamiltonian is simplified by retaining only the terms oscillating at the optical frequency scale, in accordance with the rotating wave approximation [62,63]. Specifically, all models are based on the Hamiltonian

$$\begin{aligned} H =& \hbar \sum_q \nu_q \left(b_q^\dagger b_q + \frac{1}{2} \right) + \sum_n \left(\varepsilon_{c,n} c_n^\dagger c_n + \varepsilon_{v,n} v_n^\dagger v_n \right) \\ & - i\hbar \sum_{n,q} [g_{nq} (b_q c_n^\dagger v_n + b_q v_n^\dagger c_n) \\ & - g_{nq}^* (b_q^\dagger v_n^\dagger c_n + b_q^\dagger c_n^\dagger v_n)]. \end{aligned} \tag{1}$$

ν_q is the frequency of a photon in the qth mode and g_{nq} is the light-matter coupling strength between a photon in the qth mode and the nth quantum dot. This is proportional to laser mode amplitude and the interband matrix elements and inversely proportional to the square root of mode volume and the dielectric function [68]. The bosonic operators b_q, $b_q^\dagger$ annihilate and create a photon in the qth mode, respectively, and the fermionic operators v_n, $v_n^\dagger$ (c_n, $c_n^\dagger$) annihilate and create an electron in the lower (upper) energy level of the nth quantum dot. The summation over q accounts for both lasing and nonlasing modes. In this work, we focus on nanolasers with a single lasing mode; hence, we omit the mode index. Following Ref. [61], the contributions from nonlasing modes are adiabatically eliminated and result in radiative decay. The free-electron part of the Hamiltonian describes charge carriers in the conduction- and valence-band states of the nth quantum dot, with corresponding energies $\epsilon_{c,n}$ and $\epsilon_{v,n}$, together with the photons across all modes. Phonon scattering is modeled by introducing a dephasing term $\mu\gamma$, where γ is the dephasing rate of the polarization and $\mu \geqslant 0$, applied to the electron-electron expectation values. This approach follows the methodology of Ref. [68], where it was demonstrated that such a dephasing term effectively captures the essential features of a microscopic theory of phonon scattering. Physically, phonon scattering increases the decay rate of the coherence between wave functions of carriers confined in different quantum dots, compared to those within the same quantum dot. The remaining control parameters are consistent across all models and include the decay rate of the upper level population due to nonradiative processes, γ_{nr}, which lead to intracavity absorption, and the emission into nonlasing modes, γ_{NL}; the pump rate per emitter, r; and the number of QDs N within the laser cavity. All parameter values have been selected based on experimental considerations (see Ref. [66] and Appendix E), and are summarized in Table I. In the simulations, all parameters are rescaled with respect to the nonradiative decay rate, since this rate is determined solely by the material properties and is independent of the laser cavity. This normalization is theoretically convenient because it allows for direct comparison of different cavities under the assumption of identical material characteristics. Photon creation and annihilation are represented by the bosonic operators $b^\dagger$, b, respectively, while the fermionic operators $c^\dagger$, c and $v^\dagger$, v correspond to electron creation and annihilation in

TABLE I. Model parameters, their meaning, and typical values used in the simulations. In the cases of different quantum dots the detunings $\Delta\nu_k$ are sampled from a normal distribution with zero mean and standard deviation with typical value equal to γ. The parameter values used in the simulations are those reported here unless otherwise stated in the corresponding figure caption.

Symbol	Meaning	Typical value
γ	Polarization dephasing rate	1×10^{13} s^{-1}
γ_c	Laser mode decay rate	1×10^{10} s^{-1}
γ_l	Spontaneous emission rate in the cavity mode	9.7×10^{8} s^{-1}
γ_{NL}	Decay rate in nonlasing modes	$\gamma_{\mathrm{NL}} = \gamma_l(1-\beta)/\beta$
γ_{nr}	Nonradiative decay	1×10^{9} s^{-1}
β	Spontaneous emission factor	1
$\Delta\nu$	Quantum-dot detuning (identical quantum dots)	0 s^{-1}
$\Delta\nu_k$	Detuning of the kth quantum dot	
g	Light-matter coupling strength	7×10^{10} s^{-1}
μ	Phonon scattering parameter	0
N	Number of quantum dots	50
r	Pump rate per emitter	2×10^{14} s^{-1}
w_{QD}	Standard deviation of the detuning of a QD sample	γ

the upper and lower energy levels, respectively. For a clear physical interpretation of the theory, it is essential to associate these operators with individual particles: $b^\dagger, b$ are single-particle bosonic operators, while the fermionic single-particle quantities [69] are constructed from bilinear combinations of operators, such as the electron number in the upper level, $c^\dagger c$, and the standard polarization between levels, $c^\dagger v$.

The derivation of all models begins with the Hamiltonian in Eq. (1), from which we obtain the Heisenberg equations for all operators up to three particles. From these equations, we determine the time evolution of the corresponding expectation values. These are then decomposed into sums of three-particle correlations and products of single- and two-particle expectation values. Different models arise by applying distinct levels of approximation to this decomposition, as outlined below. The TPM model [66] accounts for all two-particle quantum correlations, including photon-photon, photon-electron, and electron-electron interactions. A simplified variant, $\mathrm{TPM}_{1\mathrm{F}}$, assumes negligible electron-electron correlations and includes only electron-photon and photon-photon expectation values, truncating fermions and bosons at different levels on the basis of different decay rates, as suggested in Ref. [70]. This approximation is valid for many systems characterized by strong dephasing and high cavity quality factors [61,71]. For example, Fig. 7 in Appendix C indicates that the laser threshold predicted by the full TPM converges to that of $\mathrm{TPM}_{1\mathrm{F}}$ when phonon scattering is incorporated phenomenologically via dephasing, following the approach in Ref. [68]. In contrast, the CIM model retains only nonoscillating two-particle expectation values, consistent with typical semiclassical treatments.

We examine the impact of polydispersity in QDs on these models, assuming the QDs exhibit varying detunings that follow a Gaussian distribution centered at zero. The degree of polydispersity is characterized by the standard deviation w_{QD} of this distribution. The generalized models accounting for polydisperse QDs are denoted with a superscript (d). From a computational standpoint, it is important to note that the number of equations scales linearly with the number of QDs in the $\mathrm{CIM}^{(\mathrm{d})}$ and $\mathrm{TPM}^{(\mathrm{d})}_{1\mathrm{F}}$, whereas it scales quadratically in the $\mathrm{TPM}^{(\mathrm{d})}$.

III. THRESHOLD ANALYSIS FOR IDENTICAL QUANTUM DOTS

To enable analytical insights and extensive numerical analysis, we first consider a system of identical QDs. This assumption allows us to derive threshold conditions as functions of key parameters for CIM, TPM, and $\mathrm{TPM}_{1\mathrm{F}}$ equations. In this section we consider the threshold for self-sustained continuous stimulated emission, which is theoretically found identifying the onset of steady-state solutions with coherent variables different from zero. It is worth recalling that in nanolasers this is not the only way to define a laser threshold, with the nonuniqueness of the threshold associated to the gradual transition from incoherent to coherent emission typical of nanolsers. The threshold we consider identifies the end of this transition and requires the use of coherent variables such as the field amplitude $\langle b\rangle$, while the threshold defined in Ref. [72] identifies the onset of this transition and can be obtained with simpler models. The threshold expressions for CIM and TPM have been previously reported in Ref. [66].

Numerical simulations show that the population of the upper laser level, $\langle c^\dagger c\rangle$, is very similar in all these models. Using this property, in the TPM we can leverage the CIM's analytical value of the population at threshold to obtain an approximate expression for the threshold pump rate, as the dominant effect in this model is provided by slowly varying electron-electron expectation values. However, this strategy does not extend to the $\mathrm{TPM}_{1\mathrm{F}}$ because this model does not contain electron-electron expectation values and the dynamics below threshold is the same as the CIM dynamics. For $\mathrm{TPM}_{1\mathrm{F}}$, we instead determine the threshold numerically by integrating the dynamical equations (C2) and identifying the smallest value of the pump parameter r for which the equilibrium solution satisfies $|\langle b\rangle| \not\equiv 0$.

Figures 1(a) and 1(b) present the threshold pump rate as a function of the coupling coefficient g, along with the CIM population inversion at threshold. The inversion curves for TPM and $\mathrm{TPM}_{1\mathrm{F}}$ closely match the CIM values. As expected, $\langle c^\dagger c\rangle$ decreases monotonically with g, since stronger coupling enables the electromagnetic field to extract energy more efficiently from the excited state [Fig. 1(c)].

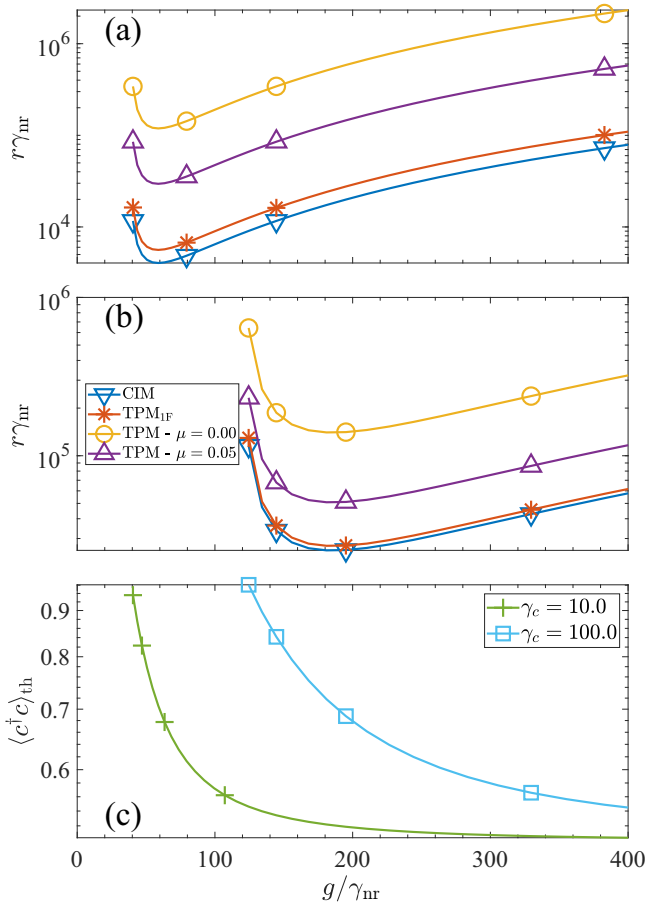

FIG. 1. Pump r at threshold for $\gamma_c = 10$ (a) and $\gamma_c = 100$ (b) as a function of the coupling coefficient g in models with identical quantum dots, CIM, $\rm TPM_{1F}$, and TPM with $\mu = 0, 0.05$ as indicated in the legend in panel (b). Panel (c) shows the CIM population of the upper level, $\langle c^\dagger c\rangle_{\rm th}$, at threshold for the corresponding values of γ_c. All parameters are as in Table I except $N = 70$, $\beta = 7 \times 10^{-4}$.

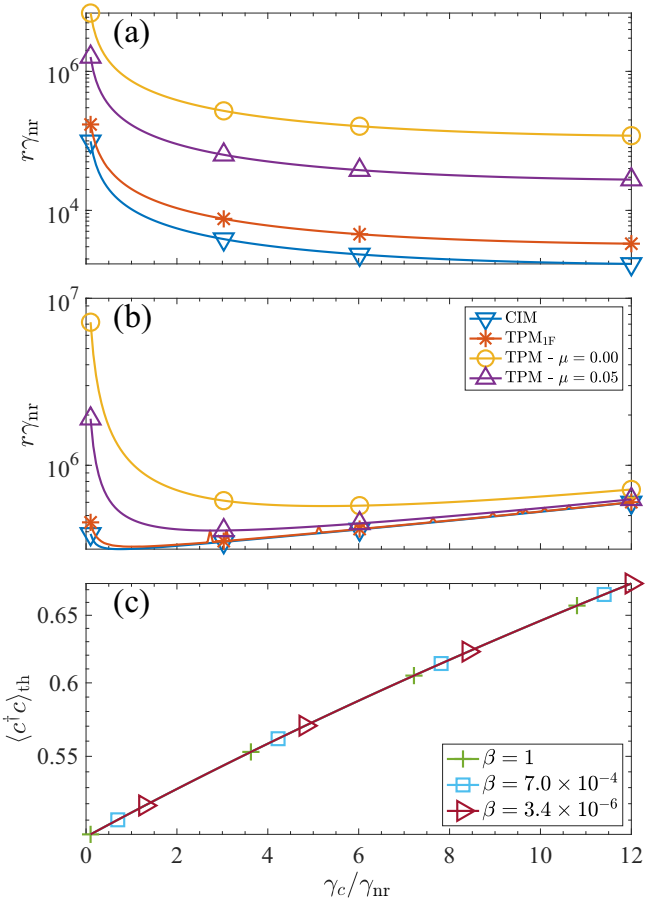

FIG. 2. Threshold value of the pump as a function of the cavity decay rate γ_c for $\beta = 1$ (a) and $\beta = 3.4 \times 10^{-6}$ (b). Panel (c) shows the CIM population of the upper level, $\langle c^\dagger c\rangle_{\rm th}$, at threshold for the corresponding values of β. All other parameters are as in Table I.

The pump threshold curve exhibits a minimum as a function of g. For small g, the coupling is too weak to effectively compensate for cavity losses. As g increases, the field becomes more effective at depleting the population inversion, eventually quenching it to lower equilibrium levels, as shown in the lower panel of Fig. 1. This necessitates stronger pumping to reach the lasing threshold, hence increasing the threshold at high g.

In Fig. 2 we explore how the threshold pump rate varies with the cavity loss rate γ_c, across different cavity sizes parametrized by the coefficient β, the spontaneous emission factor. In all cases [see Fig. 2(c)], the threshold population inversion $\langle c^\dagger c\rangle$ increases monotonically with γ_c, as higher cavity losses demand a larger inversion to sustain lasing. Notably, the population inversion curves remain essentially the same across all values of β, indicating that this dependency is largely geometry independent.

In all cases, the threshold pump rate increases as γ_c decreases to zero, i.e., as the cavity losses become smaller and smaller. This behavior results from stronger intracavity fields accelerating the depopulation processes, thereby requiring increased optical pumping to maintain sufficient inversion for lasing. For nanolasers, $\beta = 1$ [Fig. 2(a)], this is the only observable behavior in the γ_c range studied. Microlasers, e.g., $\beta = 7 \times 10^{-4}$, have nearly identical behavior (diagram not shown). In the macroscopic case, $\beta = 3.4 \times 10^{-6}$ [Fig. 2(b)], the threshold curve has a minimum. For losses larger than this value we observe also a more "standard" behavior, namely that the threshold increases with increasing losses.

It is important to note that the threshold analyzed here applies specifically to continuous wave lasing. Control parameter regions below this threshold cannot support continuous laser emission, though they may still exhibit time-dependent or pulsed lasing behavior. A detailed exploration of this possibility is left for future work.

IV. EFFECT OF POLYDISPERSE QUANTUM DOTS

The TPM and $\rm TPM_{1F}$ models show bistability between incoherent emission and coherent lasing as illustrated in Fig. 3. As a result of two-particle quantum correlation, two lasing solutions, one stable and the other unstable, appear through a saddle-node bifurcation, in stark contrast with all other laser models. As the effect of phonon scattering is increased, the TPM threshold approaches the $\rm TPM_{1F}$ threshold (see Fig. 7 in Appendix C), confirming that this model is qualitatively the

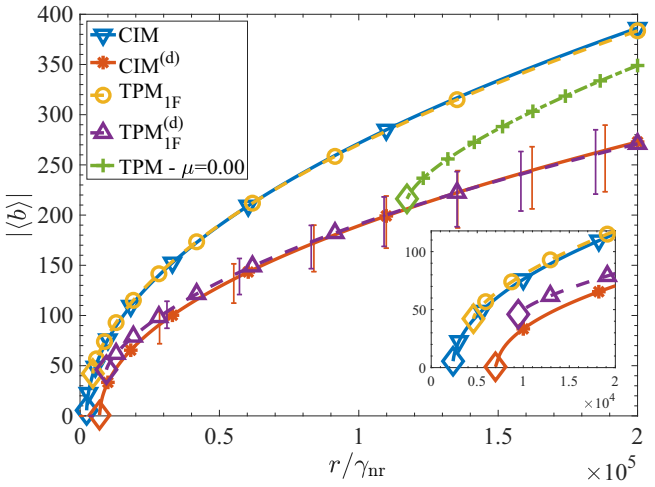

FIG. 3. Plot of the CIM and $\mathrm{TPM}_{1\mathrm{F}}$ coherent field amplitude in the lasing solution with identical (no superscript) or different [superscript $^{(\mathrm{d})}$] QDs. The $\mathrm{CIM}^{(\mathrm{d})}$ and $\mathrm{TPM}^{(\mathrm{d})}_{1\mathrm{F}}$ plots are those of sample S_3. The error bars represent the range of values measured over the ten samples. Also included for reference is the TPM amplitude with $\mu = 0$. The inset is a magnification of the low pump region. The approximate location of the lasing threshold is indicated by the large diamond symbols. All other parameters are as in Table I.

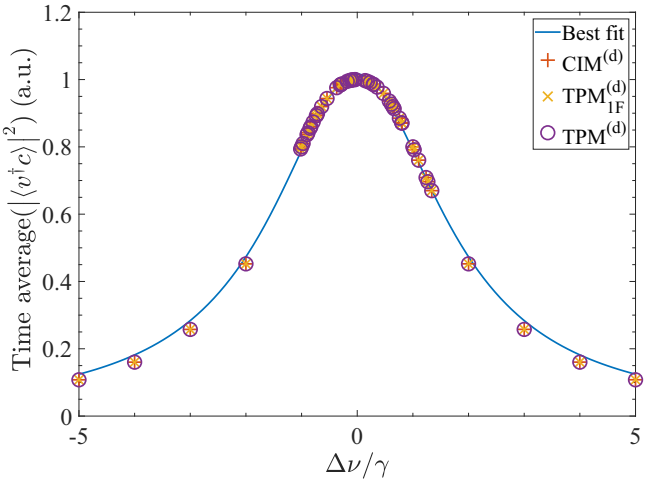

FIG. 4. Activation curve of the QDs. The markers represent the time average of $|\langle v^\dagger c\rangle|^2$, scaled in the range [0,1], computed using the CIM (plusses), $\mathrm{TPM}_{1\mathrm{F}}$ (crosses), and TPM (circle) equations at pump $r = 2 \times 10^{14}\ \mathrm{s}^{-1}$ for sample S_3. This is the rightmost point in the $\mathrm{CIM}^{(\mathrm{d})}$ and $\mathrm{TPM}^{(\mathrm{d})}_{1\mathrm{F}}$ curves in Fig. 3 and all parameter values are as in this figure. The solid line is the best fit with the Lorentzian function (2). The fitted parameters are $a_L = 1.016$ and $w_L = 1.864$.

high-temperature limit of the TPM. Despite these qualitative similarities, the TPM model has a much larger number of equations than the $\mathrm{TPM}_{1\mathrm{F}}$ when one considers polydisperse QDs. As a result of the large number of equations and the difference in the scales of the decay rates, the TPM model shows extremely long transients and for this reason we consider the effect on polidisperse QDs only on the CIM and $\mathrm{TPM}_{1\mathrm{F}}$ thresholds and perform only limited TPM simulations.

To investigate the impact of inhomogeneity, we have assumed that the QDs have identical gain g but different detunings $\Delta\nu_l$. These are random and follow a normal distribution with zero average and standard deviation w_{QD} equal to γ. We have generated ten samples, S_j, $j = 1, \ldots, 10$, of 50 QDs and have run the same simulations for each sample, keeping all the other parameters constant. In the presence of detuned QDs, the bifurcation diagrams show a shift in the lasing threshold and changes in the coherent field amplitude, but otherwise maintain their structure (Fig. 3). The error bars in Fig. 3 reflect the variability in $|\langle b\rangle|$ across the ten sampled configurations.

Figure 4 displays the normalized activity distribution—i.e., the distribution of the time average of $|\langle v_l^\dagger c_l\rangle|^2$ for the different QDs, $l = 1, 2, \ldots, n$, scaled in the range [0,1]—for sample S_3. This represents the effect of the detuning on the QD activity. The polarization amplitudes computed from the three models, rescaled to the range [0,1], overlap perfectly, confirming consistent polarization dynamics. These data are well fitted by the Lorentzian function,

$$f(\Delta\nu) = \frac{a_L}{1 + (\Delta\nu/w_L)^2}, \tag{2}$$

where a_L is the maximum of $|\langle v^\dagger c\rangle|^2$ and w_L is the width of the activation curve (solid line in Fig. 4).

An additional effect of QD detuning is the emergence of single-frequency temporal oscillations in the coherent field (see Fig. 11 in Appendix I), showing that synchronization of QDs with diverse resonant frequencies is the mechanism responsible for the emergence of a coherent field across the QD ensemble. The oscillation frequency ω and the activation curve width w_L depend on the specific QD sample but are invariant with respect to pump values above the threshold. All three models predict similar oscillation frequencies and activation curve width (see Fig. 5). A more detailed investigation of the activation curves is presented in Appendix H. As a general trend, samples with narrower detuning distributions (i.e., smaller values of the detuning standard deviation $\overline{w}$,) exhibit

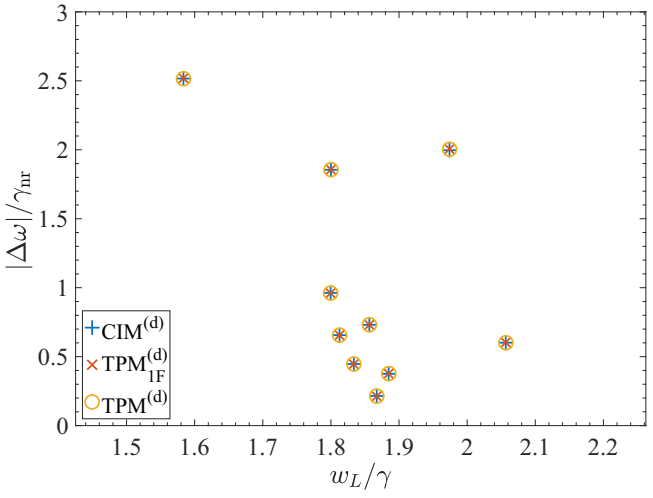

FIG. 5. Quantum-dot activation curve width w_L plotted against the angular frequency of the coherent field amplitude $\langle b\rangle$ on the CIM (plusses), $\mathrm{TPM}_{1\mathrm{F}}$ (crosses), and TPM (circles) lasing branch. The samples and all other parameters are the same as in Fig. 3 except for $r = 2 \times 10^{14}\ \mathrm{s}^{-1}$.

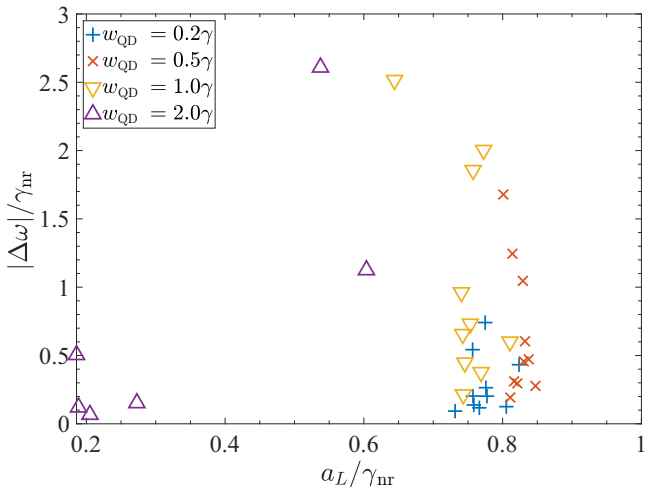

FIG. 6. Analysis of the effect of the width of the QD distributions for TPM$^{(d)}$. We report the fitted amplitude of the activation curve, a_L, and the angular frequency shift of the lasing solution, $|\Delta\omega|$, with respect to the cavity frequency for ten samples of $N = 50$ QDs. Each sample is taken from a normal distribution with zero average and standard deviation w_{QD} equal to 0.2γ (plus signs), 0.5γ (crosses), γ (downward triangles), and 2γ (upward triangles). The samples and all other parameters are the same as in Fig. 5.

broader activation curves. Conversely, samples with broader distributions display narrower activation curves. In the case of narrow distributions, most quantum dots are active, leading to higher overall system energy. This, in turn, affects the fixed number of quantum dots we impose with higher detuning, effectively raising their energy and broadening the activation curve. By contrast, in broader distributions, fewer quantum dots are maximally active, and those in the distribution tails carry less energy, which results in narrower activation curves.

Figures 4 and 5 confirm that TPM$_{1F}$ accurately reproduces the coherent polarization dynamics of TPM, differing only in the amplitude of the coherent fields, as also shown in the bifurcation diagrams (Fig. 3).

The influence of the width w_{QD} of the QD detuning distribution is further analysed in Fig. 6 where we plot the amplitude a_L of the activation curve versus the frequency shift $|\Delta\omega|$ of the lasing solution with respect to the cavity frequency for the TPM$^{(d)}$. The figure shows the outcome of the simulation of ten batches of $N = 50$ QDs sampled from distributions with widths $w_{QD} = [0.2, 0.5, 1.0, 2.0]\gamma$. From these we can see that the effect of w_{QD} on the amplitude is significant only for the largest value of w_{QD}. In this case the model is close to threshold and the fluctuations in the detunings of the QDs have a significant effect in how much the laser is above threshold. In fact, four of the $w_{QD} = 2\gamma$ simulations are below threshold. On the other hand, w_{QD} has only limited effect on the lasing frequency: the spread of frequency shift $|\Delta\omega|$ increases roughly by a factor of 2 when w_{QD} increases from 0.2γ to 0.5γ, but quickly saturates for higher values of w_{QD}. In Appendix H we give the same curve for CIM$^{(d)}$ and TPM$^{(d)}_{1F}$. The points are more scattered for the TPM$^{(d)}$ case with respect to the other two because of the larger numerical noise in the estimation of the amplitude equilibrium value for this model (see Appendix A). An analysis of the fit of the activation curve as a function of w_{QD} can be found in Appendix E.

V. CONCLUSIONS

We have used different modeling choices to analyze the laser's threshold behavior at various scales and as a function of radiation-matter coupling, cavity lifetime, and the inhomogeneous broadening inherent in the medium. At the semiclassical level, we used the CIM. Two-particle correlations were introduced with or without phonon relaxation (phenomenologically modeling temperature effects) and with a reduced set of equations, in which the fast relaxation of electron-electron correlations was heuristically taken into account.

For homogeneous broadening, we observe the anticipated threshold reduction when radiation-matter coupling weakens due to reduced conversion of population into photons. The results are qualitatively consistent across all models, exhibiting a threshold increase that accompanies the description of correlations. However, the threshold increases again below an optimum value due to the difficulty of transferring energy to the field to establish coherence when the coupling becomes too small. This effect is expected when considering the radiation-matter coupling constant g as the control parameter. We remark that the threshold we used identifies the onset of stable coherent emission with constant amplitude that, for CIM, corresponds to the end of the gradual transition to coherent emission in nanolasers [65]. The threshold defined in Ref. [72] instead identifies the beginning of that transition (see Fig. 5, bottom panel, of Ref. [72]). These two thresholds have a different behavior for large g that is the result of the extended transition to coherence in nanolasers [65]. Similarly, the pump threshold value monotonically increases with growing outcoupling losses, except in the macroscopic cavity regime where a minimum is found, followed by threshold growth in the extremely good cavity limit. Since loss values for this occurrence are outside the usual range of experimental devices, this prediction cannot be compared to observations at this stage.

Inhomogeneous broadening plays an unavoidable role in all devices. Despite considerable progress achieved in recent years, even the best fabrication processes cannot yet provide QDs with resonance frequencies well within their natural linewidth [48]. Therefore, the influence of inhomogeneous broadening on the physical properties of emission remains paramount. This investigation reveals that, with broadening amounts compatible with current devices, the differences are small and remain solely quantitative, while the emission's physical characteristics remain qualitatively the same. In all models for which we could analyze the bifurcation diagrams, inhomogeneous broadening shifted the threshold to larger values, but did not change the nature of the bifurcation, pitch-fork, and saddle node for CIM and TPM$_{1F}$ respectively. Depending on the realization of a random ensemble of QDs, the results vary slightly but remain consistent throughout, suggesting that they are robust with respect to the level of approximation chosen for the description of the causes of the inhomogeneous broadening.

These simulations address longstanding questions that have perplexed the experimental community in the face of the inevitable amount of size dispersion in QDs, which leads to a distribution of resonance frequencies [48]. In practice, we can be confident that the consequences of inhomogeneous broadening are limited to a reasonable, physically acceptable reduction in gain, which the models can quantify without additional physical consequences. While progress in QD positioning and physical size control is welcome, our results confirm that manufacturing quality is already sufficient for reliable devices.

One interesting open question is how field coherence is established in the presence of inhomogeneous broadening. Its quantification, through field autocorrelation [64], remains an open question due to the slow variation introduced by the distribution of resonance frequencies in the QDs (Fig. 11 in Appendix I). It remains to be seen how this oscillation affects the coherence length (or time). On this topic, it is worth noting that second-order correlation (photon-statistics) measurements have also been employed to probe the nature of the emission (see Ref. [60]). When the Siegert relation holds, the relationship between first- and second-order correlations becomes direct and well defined. Although we intend to extend our analysis to include second-order autocorrelation calculations, the full scope and computational demands of such an evaluation lie beyond the limits of the present work.

Finally, in this study we restrict our analysis to steady-state behavior and do not consider transients. Relaxation oscillations—arising in the transient response following a step change in a parameter—are determined by system parameters, the initial steady state, and the chosen model. Consequently, exploring the frequencies and damping timescales of these oscillations represents a promising direction for future work, offering both new insights into nanolaser physics and valuable tests for theoretical models.

ACKNOWLEDGMENTS

G.L.L. and F.P. wish to acknowledge support from AFOSR/IOE Grant No. FA8655-24-1-7017. The authors acknowledge the use of the IRIDIS High Performance Computing Facility and associated support services at the University of Southampton, in the completion of this work.

DATA AVAILABILITY

The data that support the findings of this article are not publicly available. The data are available from the authors upon reasonable request.

APPENDIX A: NUMERICAL METHODOLOGY

The number of real equations, $N_{\rm eq}$, for the CIM$^{(\rm d)}$, TPM$^{(\rm d)}_{\rm 1F}$, and TPM$^{(\rm d)}$ grows with the number N of QDs as

$$\begin{aligned} \text{CIM}^{(\rm d)} &: N_{\rm eq} = 3 + 5N, \\ \text{TPM}^{(\rm d)}_{\rm 1F} &: N_{\rm eq} = 3 + 9N, \\ \text{TPM}^{(\rm d)} &: N_{\rm eq} = 3 + 9N + 7N(N-1). \end{aligned} \tag{A1}$$

Because of the difference in magnitude between the different loss terms in the models, the equations are stiff and are integrated using the MATLAB stiff solver ODE15S. In order to reduce the computation time we provide to the solver the sparsity matrix of the Jacobian, i.e., the list of elements of the Jacobian of the model equation that are not identically zero. In the TPM$^{(\rm d)}_{\rm 1F}$ we provide the analytical Jacobian, but the increase of code speed (approximately 25%) is not large enough to code the analytical Jacobian of the much more involved TPM$^{(\rm d)}$ equations.

To produce the bifurcation diagrams, the pump parameter was set at its highest value and decreased gradually. At each change of the pump parameter, the transient was deemed to have ended when the derivatives of $|\langle b\rangle|$, $\langle b^\dagger b\rangle$, $\langle c^\dagger c\rangle$, and, if relevant, $|\langle bb\rangle|$ were smaller than a user specified parameter, normally 10^{-5}. Once equilibrium had been reached a shorter run with very fine output was produced to estimate the equilibrium values of the fields. The codes to perform the time integration of all the models and to produce the bifurcation diagrams are available on GitHub [73].

The activation curve plots for all models, except the TPM$^{(\rm d)}$, were obtained by integrating the transient for a time long enough to reach equilibrium (1000 time units), followed by a shorter integration (200 time units) with finely sampled output. This allowed the accurate determination of the asymptotic amplitude of the coherent field $\langle b\rangle$ and of its frequency.

This approach was not feasible in the TPM$^{(\rm d)}$ case, due to the slowness of the integration code. We integrated each QD sample for each detuning width $w_{\rm QD}$ for at least 100 time units, reaching nearly 500 for sample S_3. We then fitted to $\langle b\rangle$ a decaying sinusoidal function

$$f(t) = \left(a_\infty + be^{-ct}\right)\cos(\omega_\infty t + \phi), \tag{A2}$$

and used a_∞ and ω_∞ as estimates of the asymptotic amplitude and frequency of the lasing solution. We checked the convergence of these two parameters by fitting the data over increasing integration window sizes. ω_∞ had converged to at least three significant digits. The convergence of a_∞ was more tentative, as this parameter is more sensitive to the length of the integration window and to the fact that the asymptotic decay may have more than one timescale. Even in the best case the estimate of this parameter was still changing on its second digit with the increase of the integration window, suggesting that the error is of the order of a few percents.

APPENDIX B: TPM EQUATIONS

Note that the codes to perform the time integration of all the models and to produce the bifurcation diagrams are available on GitHub [73].

The starting point of the derivation of the model is to obtain from the Hamiltonian given in Eq. (1) of the main text the Heisenberg equations of the three-particle operators. Their expectation values are then decomposed in terms of the sum of the three-particle correlations and products of single- and two-particle expectation values:

$$\langle O_i O_j O_k\rangle = \langle O_i O_j O_k\rangle_{\mathcal{C}} + \langle O_i O_j O_k\rangle_{\mathcal{D}}, \tag{B1}$$

where the labels $\mathcal{C}, \mathcal{D}$ stand for correlated three-particle processes (or "connected" in terms of Feynman diagrams) and

decorrelated products of one- and two-particle processes (or "disconnected"), with

$$\langle O_iO_jO_k\rangle_{\mathcal{D}} = \langle O_i\rangle\langle O_jO_k\rangle + \langle O_j\rangle\langle O_iO_k\rangle + \langle O_k\rangle\langle O_iO_j\rangle - 2\langle O_i\rangle\langle O_j\rangle\langle O_k\rangle. \tag{B2}$$

Similarly, for the expectation values of four-particle operators we have

$$\langle O_iO_jO_kO_l\rangle = \langle O_iO_jO_kO_l\rangle_{\mathcal{C}} + \langle O_iO_jO_kO_l\rangle_{\mathcal{D}}, \tag{B3}$$

where

$$\begin{aligned}\langle O_iO_jO_kO_l\rangle_{\mathcal{D}} = {}& \langle O_i\rangle\langle O_jO_kO_l\rangle + \langle O_j\rangle\langle O_iO_kO_l\rangle + \langle O_k\rangle\langle O_iO_jO_l\rangle + \langle O_l\rangle\langle O_iO_jO_k\rangle + \langle O_iO_j\rangle\langle O_kO_l\rangle \\ & + \langle O_iO_k\rangle\langle O_jO_l\rangle + \langle O_iO_l\rangle\langle O_jO_k\rangle - 2\big(\langle O_i\rangle\langle O_j\rangle\langle O_kO_l\rangle + \langle O_iO_j\rangle\langle O_k\rangle\langle O_l\rangle + \langle O_i\rangle\langle O_k\rangle\langle O_jO_l\rangle \\ & + \langle O_iO_k\rangle\langle O_j\rangle\langle O_l\rangle + \langle O_i\rangle\langle O_l\rangle\langle O_jO_k\rangle + \langle O_iO_l\rangle\langle O_j\rangle\langle O_k\rangle\big) + 6\langle O_i\rangle\langle O_j\rangle\langle O_k\rangle\langle O_l\rangle.\end{aligned} \tag{B4}$$

Including all two-particle expectation values [66] and truncating the infinite hierarchy of expectation values by neglecting three-particle correlations, in the rotating frame we find the TPM$^{(d)}$ equations:

$$d_t\langle b\rangle = -\gamma_c\langle b\rangle + \sum_n g_n^*\langle v_n^\dagger c_n\rangle, \tag{B5a}$$

$$d_t\langle v_l^\dagger c_l\rangle = -(\gamma - i\Delta\nu_l)\langle v_l^\dagger c_l\rangle + g_l(2\langle bc_l^\dagger c_l\rangle - \langle b\rangle), \tag{B5b}$$

$$d_t\langle c_l^\dagger c_l\rangle = r(1-\langle c_l^\dagger c_l\rangle) - (\gamma_{\rm NL}+\gamma_{\rm nr})\langle c_l^\dagger c_l\rangle - 2{\rm Re}(g_l\langle bc_l^\dagger v_l\rangle), \tag{B5c}$$

$$d_t\langle b^\dagger b\rangle = -2\gamma_c\langle b^\dagger b\rangle + 2\sum_n {\rm Re}(g_n\langle bc_n^\dagger v_n\rangle), \tag{B5d}$$

$$\begin{aligned}d_t\langle bc_l^\dagger v_l\rangle = {}& -(\gamma+\gamma_c+i\Delta\nu_l)\langle bc_l^\dagger v_l\rangle + g_l^*[\langle c_l^\dagger c_l\rangle - \langle b^\dagger b\rangle(1-2\langle c_l^\dagger c_l\rangle) - 4|\langle b\rangle|^2\langle c_l^\dagger c_l\rangle + 4{\rm Re}(\langle b\rangle\langle b^\dagger c_l^\dagger c_l\rangle)] \\ & + \sum_{n\neq l} g_n^*\langle c_l^\dagger v_n^\dagger c_n v_l\rangle,\end{aligned} \tag{B5e}$$

$$\begin{aligned}d_t\langle bc_l^\dagger c_l\rangle = {}& -(\gamma_c+\gamma_{\rm nr})\langle bc_l^\dagger c_l\rangle - \gamma_{\rm NL}\langle b\rangle\langle c_l^\dagger c_l\rangle - g_l[2\langle b\rangle(\langle bc_l^\dagger v_l\rangle - \langle b\rangle\langle c_l^\dagger v_l\rangle) + \langle bb\rangle\langle c_l^\dagger v_l\rangle] \\ & - g_l^*[\langle b^\dagger\rangle(\langle bv_l^\dagger c_l\rangle - 2\langle b\rangle\langle v_l^\dagger c_l\rangle) + \langle b^\dagger b\rangle\langle v_l^\dagger c_l\rangle + \langle b\rangle\langle b^\dagger v_l^\dagger c_l\rangle] + r\langle b\rangle(1-\langle c_l^\dagger c_l\rangle) + \sum_{n\neq l} g_n^*\langle v_n^\dagger c_l^\dagger c_l c_n\rangle,\end{aligned} \tag{B5f}$$

$$\begin{aligned}d_t\langle bv_l^\dagger c_l\rangle = {}& -(\gamma_c+\gamma-i\Delta\nu_l)\langle bv_l^\dagger c_l\rangle + g_l[-\langle bb\rangle(1-2\langle c_l^\dagger c_l\rangle) + 4\langle b\rangle(\langle bc_l^\dagger c_l\rangle - \langle b\rangle\langle c_l^\dagger c_l\rangle)] \\ = {}& + \sum_{n\neq l} g_n^*\langle v_n^\dagger v_l^\dagger c_l c_n\rangle,\end{aligned} \tag{B5g}$$

$$d_t\langle bb\rangle = -2\gamma_c\langle bb\rangle + 2\sum_n g_n^*\langle bv_n^\dagger c_n\rangle, \tag{B5h}$$

$$\begin{aligned}d_t\langle c_n^\dagger v_l^\dagger c_l v_n\rangle = {}& -[2\gamma(1+\mu) - i(\Delta\nu_l - \Delta\nu_n)]\langle c_n^\dagger v_l^\dagger c_l v_n\rangle \\ & - g_n^*[-2\langle b^\dagger\rangle\langle v_l^\dagger c_n^\dagger c_n c_l\rangle + \langle b^\dagger v_l^\dagger c_l\rangle(1-2\langle c_n^\dagger c_n\rangle) - 2\langle v_l^\dagger c_l\rangle\langle b^\dagger c_n^\dagger c_n\rangle + 4\langle b^\dagger\rangle\langle c_n^\dagger c_n\rangle\langle v_l^\dagger c_l\rangle] \\ & - g_l[-2\langle b\rangle\langle v_n^\dagger c_l^\dagger c_l c_n\rangle^* + \langle bc_n^\dagger v_n\rangle(1-2\langle c_l^\dagger c_l\rangle) - 2\langle c_n^\dagger v_n\rangle\langle bc_l^\dagger c_l\rangle + 4\langle b\rangle\langle c_l^\dagger c_l\rangle\langle c_n^\dagger v_n\rangle],\end{aligned} \tag{B5i}$$

$$\begin{aligned}d_t\langle v_n^\dagger c_l^\dagger c_l c_n\rangle = {}& -[\gamma(1+\mu)+\gamma_{\rm nr} - i\Delta\nu_n]\langle v_n^\dagger c_l^\dagger c_l c_n\rangle - g_n[-2\langle b\rangle\langle c_n^\dagger c_l^\dagger c_l c_n\rangle + 4\langle b\rangle\langle c_n^\dagger c_n\rangle\langle c_l^\dagger c_l\rangle \\ & - 2\langle c_n^\dagger c_n\rangle\langle bc_l^\dagger c_l\rangle - 2\langle c_l^\dagger c_l\rangle\langle bc_n^\dagger c_n\rangle + \langle bc_l^\dagger c_l\rangle] + g_l[-\langle b\rangle\langle c_l^\dagger v_n^\dagger c_n v_l\rangle + 2\langle b\rangle\langle v_n^\dagger c_n\rangle\langle c_l^\dagger v_l\rangle \\ & - \langle v_n^\dagger c_n\rangle\langle bc_l^\dagger v_l\rangle - \langle c_l^\dagger v_l\rangle\langle bv_n^\dagger c_n\rangle] + g_l^*[-\langle b^\dagger\rangle\langle v_n^\dagger v_l^\dagger c_l c_n\rangle + 2\langle b^\dagger\rangle\langle v_n^\dagger c_n\rangle\langle v_l^\dagger c_l\rangle \\ & - \langle v_n^\dagger c_n\rangle\langle b^\dagger v_l^\dagger c_l\rangle - \langle v_l^\dagger c_l\rangle\langle b^\dagger v_n^\dagger c_n\rangle] + r\langle v_n^\dagger c_n\rangle(1-\langle c_l^\dagger c_l\rangle) - \gamma_{\rm NL}\langle v_n^\dagger c_n\rangle\langle c_l^\dagger c_l\rangle,\end{aligned} \tag{B5j}$$

$$\begin{aligned}d_t\langle v_n^\dagger v_l^\dagger c_l c_n\rangle = {}& -[2\gamma(1+\mu) - i(\Delta\nu_n+\Delta\nu_l)]\langle v_n^\dagger v_l^\dagger c_l c_n\rangle \\ & - g_n[-2\langle b\rangle\langle v_l^\dagger c_n^\dagger c_n c_l\rangle + 4\langle b\rangle\langle c_n^\dagger c_n\rangle\langle v_l^\dagger c_l\rangle + \langle bv_l^\dagger c_l\rangle(1-2\langle c_n^\dagger c_n\rangle) - 2\langle v_l^\dagger c_l\rangle\langle bc_n^\dagger c_n\rangle] \\ & - g_l[-2\langle b\rangle\langle v_n^\dagger c_l^\dagger c_l c_n\rangle - 2\langle v_n^\dagger c_n\rangle\langle bc_l^\dagger c_l\rangle + \langle bv_n^\dagger c_n\rangle(1-2\langle c_l^\dagger c_l\rangle) + 4\langle b\rangle\langle c_l^\dagger c_l\rangle\langle v_n^\dagger c_n\rangle],\end{aligned} \tag{B5k}$$

$$\begin{aligned}d_t\langle c_n^\dagger c_l^\dagger c_l c_n\rangle = {}& -2\gamma_{\rm nr}\langle c_l^\dagger c_n^\dagger c_n c_l\rangle + 2{\rm Re}[g_n(-\langle b\rangle\langle v_n^\dagger c_l^\dagger c_l c_n\rangle^* + 2\langle b\rangle\langle c_n^\dagger v_n\rangle\langle c_l^\dagger c_l\rangle - \langle c_l^\dagger c_l\rangle\langle bc_n^\dagger v_n\rangle - \langle c_n^\dagger v_n\rangle\langle bc_l^\dagger c_l\rangle) \\ & + g_l(-\langle b\rangle\langle v_l^\dagger c_n^\dagger c_n c_l\rangle^* + 2\langle b\rangle\langle c_n^\dagger c_n\rangle\langle c_l^\dagger v_l\rangle - \langle c_n^\dagger c_n\rangle\langle bc_l^\dagger v_l\rangle - \langle c_l^\dagger v_l\rangle\langle bc_n^\dagger c_n\rangle)] \\ & + r[\langle c_l^\dagger c_l\rangle(1-\langle c_n^\dagger c_n\rangle) + \langle c_n^\dagger c_n\rangle(1-\langle c_l^\dagger c_l\rangle)] - 2\gamma_{\rm NL}\langle c_n^\dagger c_n\rangle\langle c_l^\dagger c_l\rangle.\end{aligned} \tag{B5l}$$

In these equations

$$\Delta\nu_l = \nu - \nu_{\epsilon_l}, \tag{B6}$$

with ν and ν_{ϵ_l} the frequencies of the laser mode and the radiative transition of the lth QD. g_n is the light-matter coupling coefficient of the nth QD with the sth mode, $\gamma_{\rm nr}$ is the population decay rate due to nonradiative losses, γ is the decay rate of the polarization, γ_c is the decay rate of the laser mode, and $\gamma\mu$, with $\mu \geqslant 0$, is the dephasing rate due to phonon scattering.

The equivalent equations for identical QDs are in Ref. [66], Eq. (S.14), and are reproduced here for completeness:

$$d_t\langle b\rangle = -\gamma_c\langle b\rangle + Ng^*\langle v^\dagger c\rangle, \tag{B7a}$$
$$d_t\langle v^\dagger c\rangle = -(\gamma - i\Delta\nu)\langle v^\dagger c\rangle + g(2\langle bc^\dagger c\rangle - \langle b\rangle), \tag{B7b}$$
$$d_t\langle c^\dagger c\rangle = -\gamma_{\rm nr}\langle c^\dagger c\rangle - (g\langle bc^\dagger v\rangle + \text{H.c.}) + [-\gamma_{\rm NL}\langle c^\dagger c\rangle + r(1 - \langle c^\dagger c\rangle)], \tag{B7c}$$
$$d_t\langle b^\dagger b\rangle = -2\gamma_c\langle b^\dagger b\rangle + N(g\langle bc^\dagger v\rangle + \text{H.c.}), \tag{B7d}$$
$$d_t\langle bc^\dagger v\rangle = -(\gamma + \gamma_c + i\Delta\nu)\langle bc^\dagger v\rangle + g^*[\langle c^\dagger c\rangle + 2\langle b^\dagger bc^\dagger c\rangle_{\mathcal{D}} - \langle b^\dagger b\rangle] + (N-1)g^*\langle c^\dagger v^\dagger cv\rangle, \tag{B7e}$$
$$d_t\langle bc^\dagger c\rangle = -(\gamma_c + \gamma_{\rm nr})\langle bc^\dagger c\rangle - g\langle bbc^\dagger v\rangle_{\mathcal{D}} - g^*\langle b^\dagger bv^\dagger c\rangle_{\mathcal{D}} + (N-1)g^*\langle c^\dagger v^\dagger cc\rangle + \langle b\rangle[-\gamma_{\rm NL}\langle c^\dagger c\rangle + r(1 - \langle c^\dagger c\rangle)], \tag{B7f}$$
$$d_t\langle bb\rangle = -2\gamma_c\langle bb\rangle + 2Ng^*\langle bv^\dagger c\rangle, \tag{B7g}$$
$$d_t\langle bv^\dagger c\rangle = -[\gamma_c + \gamma - i\Delta\nu]\langle bv^\dagger c\rangle + g[2\langle bbc^\dagger c\rangle_{\mathcal{D}} - \langle bb\rangle] + (N-1)g^*\langle v^\dagger v^\dagger cc\rangle, \tag{B7h}$$
$$d_t\langle c^\dagger v^\dagger cv\rangle = -2\gamma(1+\mu)\langle c^\dagger v^\dagger cv\rangle + g^*[2\langle b^\dagger v^\dagger c^\dagger cc\rangle_{\mathcal{D}} - \langle b^\dagger v^\dagger c\rangle] + g[2\langle bc^\dagger c^\dagger cv\rangle_{\mathcal{D}} - \langle bc^\dagger v\rangle], \tag{B7i}$$
$$d_t\langle v^\dagger c^\dagger cc\rangle = -[\gamma(1+\mu) + \gamma_{\rm nr} - i\Delta\nu]\langle v^\dagger c^\dagger cc\rangle + g[2\langle bc^\dagger c^\dagger cc\rangle_{\mathcal{D}} - \langle bc^\dagger c\rangle] - g\langle bc^\dagger v^\dagger cv\rangle_{\mathcal{D}} - g^*\langle b^\dagger v^\dagger v^\dagger cc\rangle_{\mathcal{D}} + \langle v^\dagger c\rangle[-\gamma_{\rm NL}\langle c^\dagger c\rangle + r(1 - \langle c^\dagger c\rangle)], \tag{B7j}$$
$$d_t\langle v^\dagger v^\dagger cc\rangle = -2[\gamma(1+\mu) - i\Delta\nu]\langle v^\dagger v^\dagger cc\rangle + 2g[2\langle bv^\dagger c^\dagger cc\rangle_{\mathcal{D}} - \langle bv^\dagger c\rangle], \tag{B7k}$$
$$d_t\langle c^\dagger c^\dagger cc\rangle = -2\gamma_{\rm nr}\langle c^\dagger c^\dagger cc\rangle - [2g\langle bc^\dagger c^\dagger cv\rangle_{\mathcal{D}} + \text{H.c.}] + 2\langle c^\dagger c\rangle[-\gamma_{\rm NL}\langle c^\dagger c\rangle + r(1 - \langle c^\dagger c\rangle)]. \tag{B7l}$$

APPENDIX C: TPM$_{1F}$ EQUATIONS

The TPM$_{1F}$ extends the CIM by including all two-particle boson-fermion and boson-boson operators. It differs from the TPM by excluding the two-particle fermion-fermion operators, Eqs. (B5i)–(B5l). The TPM$^{(d)}_{1F}$ equations—derived assuming different quantum dots—are the same as Eqs. (B5a)–(B5h) except that the two-fermion expectation values have been replaced by their truncated expansion; e.g., the term $\langle c_l^\dagger v_n^\dagger c_n v_l\rangle$ in Eq. (B5e) is replaced by $\langle c_l^\dagger v_l\rangle\langle v_n^\dagger c_n\rangle$, with $n \neq l$, in Eq. (C1e):

$$d_t\langle b\rangle = -\gamma_c\langle b\rangle + \sum_n g_n^*\langle v_n^\dagger c_n\rangle, \tag{C1a}$$
$$d_t\langle v_l^\dagger c_l\rangle = -(\gamma - i\Delta\nu_l)\langle v_l^\dagger c_l\rangle + g_l(2\langle bc_l^\dagger c_l\rangle - \langle b\rangle), \tag{C1b}$$
$$d_t\langle c_l^\dagger c_l\rangle = r(1 - \langle c_l^\dagger c_l\rangle) - (\gamma_{\rm NL} + \gamma_{\rm nr})\langle c_l^\dagger c_l\rangle - 2\text{Re}(g_l\langle bc_l^\dagger v_l\rangle), \tag{C1c}$$
$$d_t\langle b^\dagger b\rangle = -2\gamma_c\langle b^\dagger b\rangle + 2\sum_n \text{Re}(g_n\langle bc_n^\dagger v_n\rangle), \tag{C1d}$$
$$d_t\langle bc_l^\dagger v_l\rangle = -(\gamma_c + \gamma + i\Delta\nu_l)\langle bc_l^\dagger v_l\rangle + g_l^*[\langle c_l^\dagger c_l\rangle - \langle b^\dagger b\rangle(1 - 2\langle c_l^\dagger c_l\rangle) + 4\text{Re}(\langle b\rangle\langle b^\dagger c_l^\dagger c_l\rangle) - 4|\langle b\rangle|^2\langle c_l^\dagger c_l\rangle] + \langle c_l^\dagger v_l\rangle\sum_{n\neq l} g_n^*\langle v_n^\dagger c_n\rangle, \tag{C1e}$$
$$d_t\langle bc_l^\dagger c_l\rangle = -(\gamma_{\rm nr} + \gamma_c)\langle bc_l^\dagger c_l\rangle - \gamma_{\rm NL}\langle b\rangle\langle c_l^\dagger c_l\rangle - g_l(\langle c_l^\dagger v_l\rangle\langle bb\rangle + 2\langle b\rangle\langle bc_l^\dagger v_l\rangle - 2\langle b\rangle^2\langle c_l^\dagger v_l\rangle) - g_l^*(\langle v_l^\dagger c_l\rangle\langle b^\dagger b\rangle + \langle b\rangle\langle b^\dagger v_l^\dagger c_l\rangle - 2|\langle b\rangle|^2\langle v_l^\dagger c_l\rangle + \langle b^\dagger\rangle\langle bv_l^\dagger c_l\rangle) + r\langle b\rangle(1 - \langle c_l^\dagger c_l\rangle) + \langle c_l^\dagger c_l\rangle\sum_{n\neq l} g_n^*\langle v_n^\dagger c_n\rangle, \tag{C1f}$$
$$d_t\langle bv_l^\dagger c_l\rangle = -(\gamma + \gamma_c - i\Delta\nu_l)\langle bv_l^\dagger c_l\rangle + g_l[-\langle bb\rangle(1 - 2\langle c_l^\dagger c_l\rangle) + 4\langle b\rangle(\langle bc_l^\dagger c_l\rangle - \langle b\rangle\langle c_l^\dagger c_l\rangle)] + \langle v_l^\dagger c_l\rangle\sum_{n\neq l} g_n^*\langle v_n^\dagger c_n\rangle, \tag{C1g}$$
$$d_t\langle bb\rangle = -2\gamma_c\langle bb\rangle + 2\sum_n g_n^*\langle bv_n^\dagger c_n\rangle. \tag{C1h}$$

If the QDs are identical (TPM$_{1F}$) the equations become

$$d_t\langle b\rangle = -\gamma_c\langle b\rangle + Ng^*\langle v^\dagger c\rangle, \tag{C2a}$$
$$d_t\langle v^\dagger c\rangle = -(\gamma - i\Delta\nu)\langle v^\dagger c\rangle + g(2\langle bc^\dagger c\rangle - \langle b\rangle), \tag{C2b}$$
$$d_t\langle c^\dagger c\rangle = r(1 - \langle c^\dagger c\rangle) - (\gamma_{\rm NL} + \gamma_{\rm nr})\langle c^\dagger c\rangle - 2\text{Re}(g\langle bc^\dagger v\rangle), \tag{C2c}$$
$$d_t\langle b^\dagger b\rangle = -2\gamma_c\langle b^\dagger b\rangle + 2N\text{Re}(g\langle bc^\dagger v\rangle), \tag{C2d}$$
$$d_t\langle bc^\dagger v\rangle = -(\gamma_c + \gamma + i\Delta\nu)\langle bc^\dagger v\rangle + g^*[\langle c^\dagger c\rangle + (2\langle c^\dagger c\rangle - 1)\langle b^\dagger b\rangle + 4\text{Re}(\langle b\rangle\langle b^\dagger c^\dagger c\rangle) - 4|\langle b\rangle|^2\langle c^\dagger c\rangle] + g^*(N-1)\langle c^\dagger v\rangle\langle v^\dagger c\rangle, \tag{C2e}$$

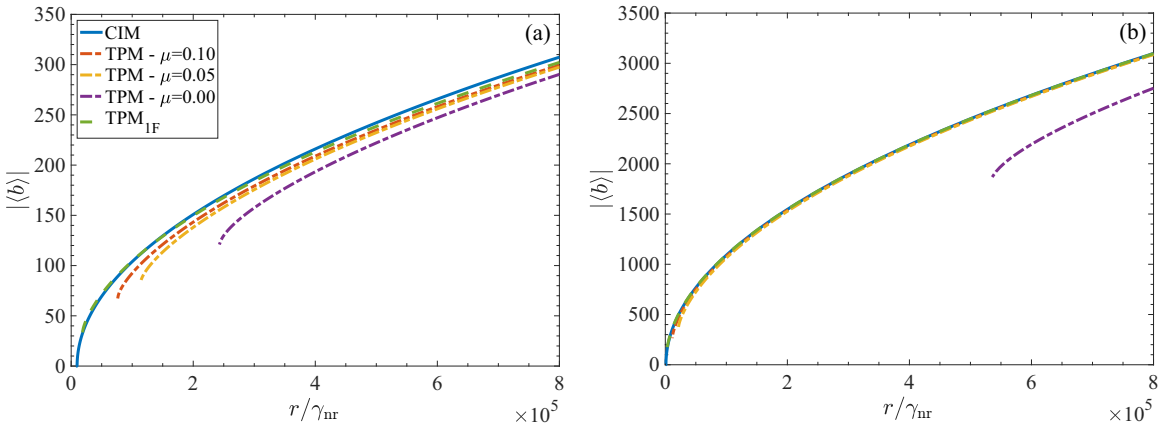

FIG. 7. Lasing solutions for the CIM (solid blue line), the TPM (dot-dashed lines, purple, yellow, and red for $\mu = [0.0, 0.05, 0.1]$ respectively), and the $\text{TPM}_{1\text{F}}$ (dashed green line) with $N = 25$ (a) and $N = 500$ (b). All other parameters are as in Table I. These are the same as in Fig. 3 of the main body of the paper, but are computed for different values of N.

$$d_t\langle bc^\dagger c\rangle = -(\gamma_{\text{nr}}+\gamma_c)\langle bc^\dagger c\rangle - \gamma_{\text{NL}}\langle b\rangle\langle c^\dagger c\rangle - g(\langle c^\dagger v\rangle\langle bb\rangle + 2\langle b\rangle\langle bc^\dagger v\rangle - 2\langle b\rangle^2\langle c^\dagger v\rangle) - g^*(\langle v^\dagger c\rangle\langle b^\dagger b\rangle + 2\langle b\rangle\langle b^\dagger v^\dagger c\rangle - 2|\langle b\rangle|^2\langle v^\dagger c\rangle + \langle b^\dagger\rangle\langle bv^\dagger c\rangle) + r\langle b\rangle(1-\langle c^\dagger c\rangle) + (N-1)g^*\langle c^\dagger c\rangle\langle v^\dagger c\rangle, \tag{C2f}$$

$$d_t\langle bv^\dagger c\rangle = -(\gamma+\gamma_c - i\Delta\nu)\langle bv^\dagger c\rangle + g[\langle bb\rangle(2\langle c^\dagger c\rangle - 1) + 4\langle b\rangle(\langle bc^\dagger c\rangle - \langle b\rangle\langle c^\dagger c\rangle)] + (N-1)g^*\langle v^\dagger c\rangle\langle v^\dagger c\rangle, \tag{C2g}$$

$$d_t\langle bb\rangle = -2\gamma_c\langle bb\rangle + 2Ng^*\langle bv^\dagger c\rangle. \tag{C2h}$$

Figure 7 indicates that the laser threshold predicted by the full TPM with identical QDs converges to that of $\text{TPM}_{1\text{F}}$ when phonon scattering is incorporated phenomenologically via dephasing, following the approach in Ref. [68].

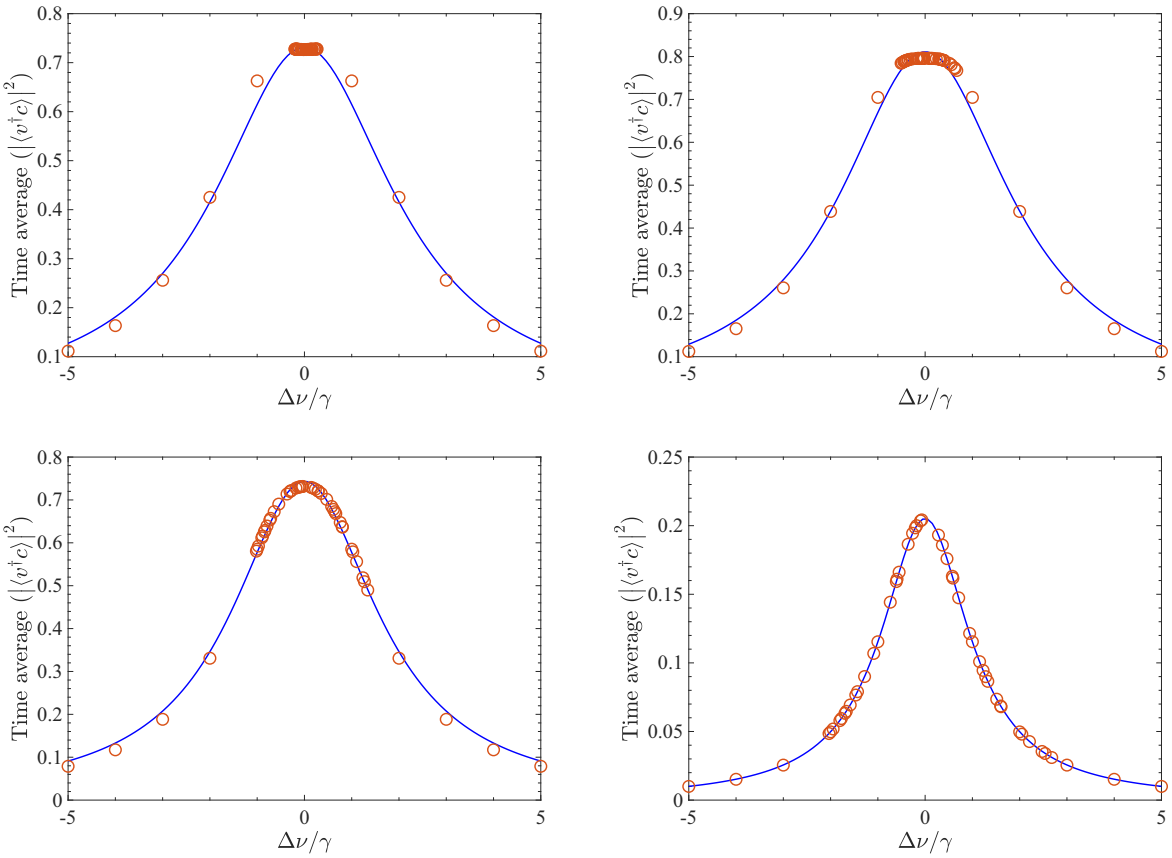

FIG. 8. Best fit of the activation curve for $w_{\text{QD}} = [0.2, 0.5, 1.0, 2.0]\gamma$ from left to right, top to bottom. Model: $\text{TPM}^{(\text{d})}$. Sample: S_3. All other parameters are as in Table I.

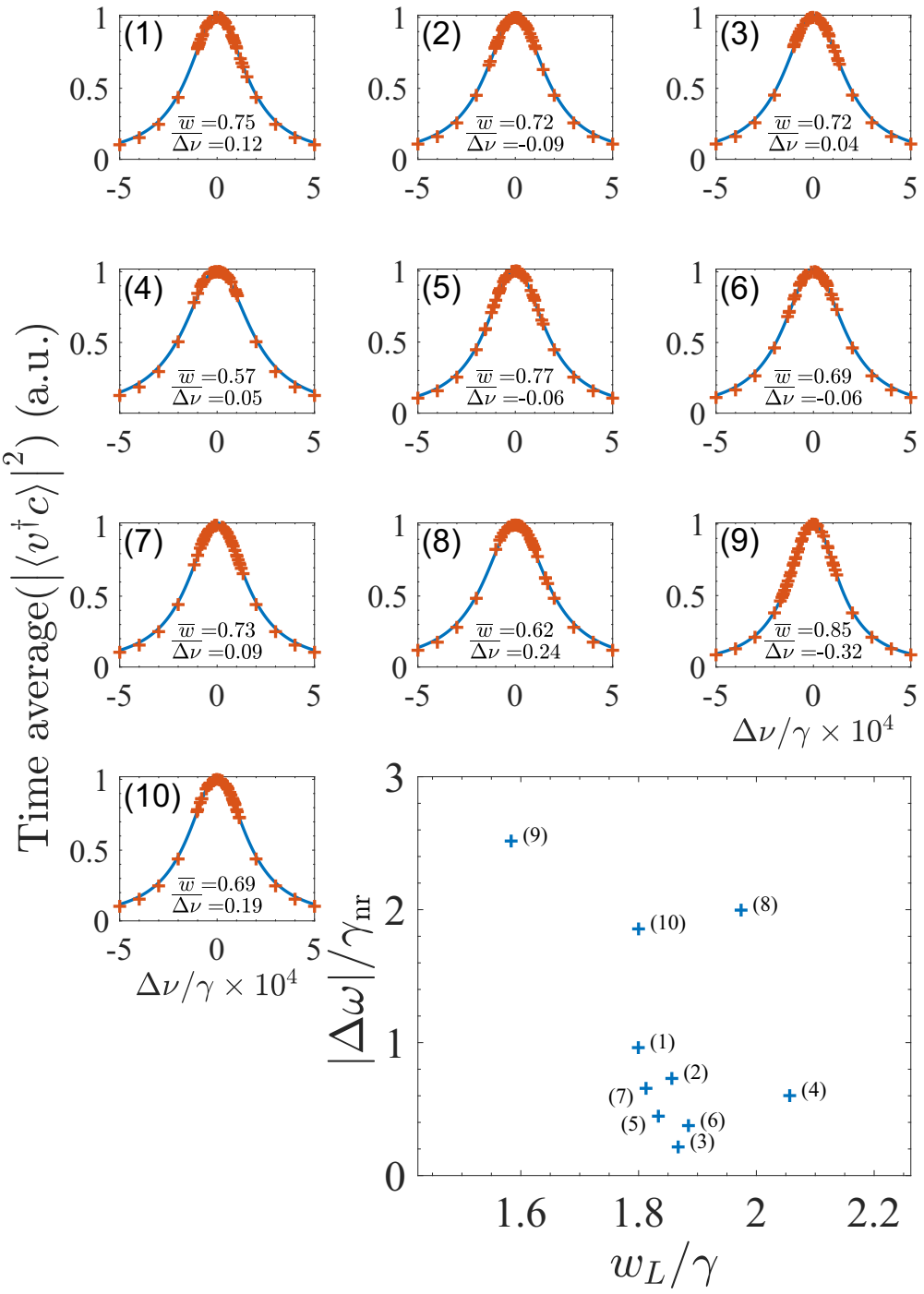

FIG. 9. The small panels, numbered 1 to 10, are the activation curves of the samples S_1 to S_{10} respectively with $w_{\rm QD} = \gamma$. The plot in the lower right quadrant is the same as Fig. 6 and represents the quantum-dot activation curve width w_L plotted against the angular frequency of the coherent field amplitude $\langle b\rangle$. The number next to each point is the sample index, e.g., the point with highest detuning is produced by sample S_9. In all panels only the CIM data are plotted for ease of visualization. All other parameters are as in Table I.

APPENDIX D: CIM EQUATIONS

The CIM$^{(d)}$ equations are Eqs. (B5a)–(B5e) suitably truncated:

$$d_t\langle b\rangle = -\gamma_c\langle b\rangle + \sum_n g_n^*\langle v_n^\dagger c_n\rangle, \tag{D1a}$$

$$d_t\langle v_l^\dagger c_l\rangle = -(\gamma - i\Delta\nu_l)\langle v_l^\dagger c_l\rangle + g_l\langle b\rangle(2\langle c_l^\dagger c_l\rangle - 1), \tag{D1b}$$

$$d_t\langle c_l^\dagger c_l\rangle = r(1-\langle c^\dagger c\rangle) - (\gamma_{\rm NL}+\gamma_{\rm nr})\langle c^\dagger c\rangle - 2{\rm Re}(g_l\langle b c_l^\dagger v_l\rangle), \tag{D1c}$$

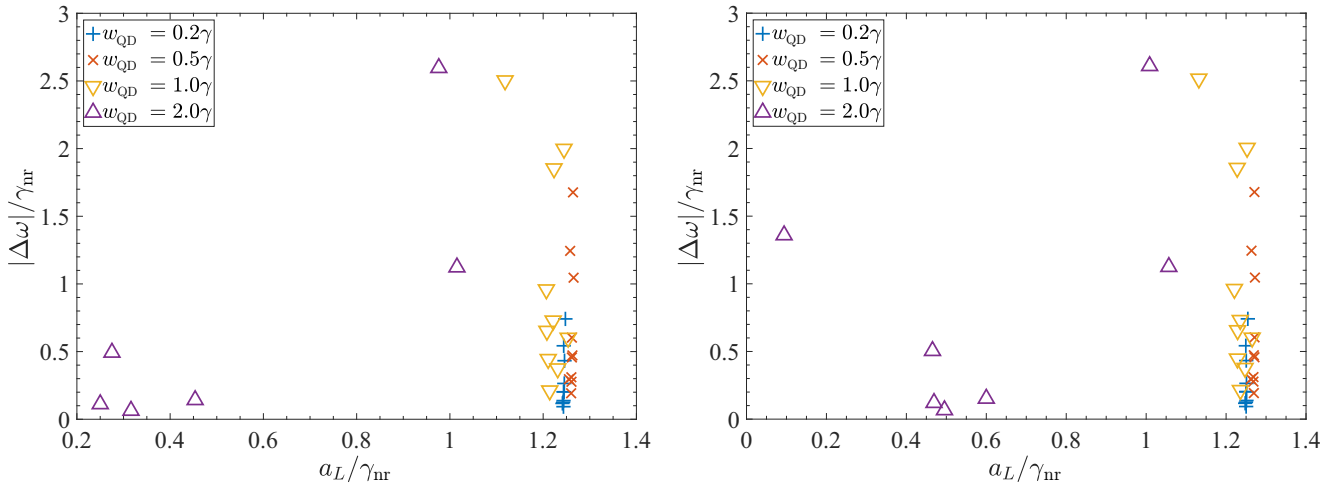

FIG. 10. Analysis of the effect of the width of the QD distributions for CIM$^{(d)}$ and TPM$^{(d)}_{1F}$ from left to right respectively. In all panels we report the fitted amplitude of the activation curve, a_L, and the angular frequency shift of the lasing solution, $|\Delta\omega|$, with respect to the cavity frequency for ten samples of $N = 50$ QDs. Each sample is taken from a normal distribution with zero average and standard deviation w_{QD} equal to 0.2γ (plus signs), 0.5γ (crosses), γ (downward triangles), and 2γ (upward triangles). The samples and all other parameters are the same as in Fig. 7.

$$d_t\langle b^\dagger b\rangle = -2\gamma_c\langle b^\dagger b\rangle + 2\sum_n \mathrm{Re}(g_n\langle bc_n^\dagger v_n\rangle), \tag{D1d}$$

$$d_t\langle bc_l^\dagger v_l\rangle = -(\gamma_c+\gamma+i\Delta\nu_l)\langle bc_l^\dagger v_l\rangle + g_l^*[\langle c_l^\dagger c_l\rangle + (2\langle c_l^\dagger c_l\rangle - 1)\langle b^\dagger b\rangle] + \sum_{n\neq l} g_n^*\langle c_l^\dagger v_l\rangle\langle v_n^\dagger c_n\rangle. \tag{D1e}$$

Equations (D1a)–(D1d) are the same as the TPMs Eqs. (B5a)–(B5d). Equations (D1e) and (B5g) differ in the coupling to the higher-order terms, which are missing in the CIM.

The equivalent equations for identical QDs are in Ref. [66], Eq. (S.15), and are reproduced here for completeness:

$$d_t\langle b\rangle = -\gamma_c\langle b\rangle + Ng^*\langle v^\dagger c\rangle, \tag{D2a}$$

$$d_t\langle v^\dagger c\rangle = -(\gamma - i\Delta\nu)\langle v^\dagger c\rangle + g\langle b\rangle(2\langle c^\dagger c\rangle - 1). \tag{D2b}$$

$$d_t\langle c^\dagger c\rangle = -(\gamma_{nr}+\gamma_{NL})\langle c^\dagger c\rangle - (g\langle bc^\dagger v\rangle + \mathrm{H.c.}) + r(1-\langle c^\dagger c\rangle), \tag{D2c}$$

$$d_t\langle b^\dagger b\rangle = -2\gamma_c\langle b^\dagger b\rangle + N(g\langle bc^\dagger v\rangle + \mathrm{H.c.}), \tag{D2d}$$

$$d_t\langle bc^\dagger v\rangle = -(\gamma+\gamma_c+i\Delta\nu)\langle bc^\dagger v\rangle + g^*[\langle c^\dagger c\rangle + \langle b^\dagger b\rangle(2\langle c^\dagger c\rangle - 1)] + (N-1)g^*\langle c^\dagger v\rangle\langle v^\dagger c\rangle. \tag{D2e}$$

APPENDIX E: EXPERIMENTAL VALUES OF QD FREQUENCY DISPERSION

Technological developments have strongly improved the size homogeneity of QDs, thus leading to closer resonance frequencies and providing samples with a moderate degree of inhomogeneous broadening. While in the early 2000s it was possible to observe frequency spreads of the order of 10% of the cavity fundamental mode (CFM), current realizations are capable of obtaining $\gtrsim 60\%$ of QDs in a frequency interval which is within 0.4% of the CFM [48]. Furthermore, Fig. 1(d) of Ref. [48] shows that even the *largest* relative spread observed in experimental samples is approximately 1.1%.

More quantitatively, the two QD populations analyzed in Fig. 1(d) of Ref. [48] have wavelength standard deviation $\Delta\lambda \simeq \{2.5, 3.6\}$ nm respectively, with central wavelength $\lambda \simeq 920$ nm. The corresponding inhomogeneous frequency spread $\Delta\nu_{in}$ of the broader population is

$$\Delta\nu_{in} = \nu\frac{\Delta\lambda}{\lambda} \simeq 1.3\times10^{12}\ \mathrm{Hz} = 1300\gamma_{nr}, \tag{E1}$$

for the value of the nonradiative transition decay rate used in all the simulations in this paper. This is equivalent to $w_{QD} \simeq 0.13\gamma$, which is on the low range of the value used in this paper.

APPENDIX F: ACTIVATION CURVES FOR DIFFERENT DETUNING WIDTHS

In order to visualize the activation curve we split the QDs in core and tail. The latter are ten QDs with preassigned detuning $\pm k\gamma$, with $k = 1, 2, \ldots, 5$. The former are the remaining 40 QDs; their detuning is randomly sampled from a normal distribution with zero average and standard deviation equal to γ. This choice of QDs detunings allows the visualization of the activation curve, but affects its fitting. In the case of $w_{QD} = 0.2\gamma$ (top left panel of Fig. 8), all the core QDs are equally active and feed energy quite effectively to the tail QDs, resulting in a rather wide activation curve which, however, is more the result of the chosen QD distribution than of the nanolaser physics. This is also hinted at by the relatively poor fit of the Lorentzian function to the numerical data.

As w_{QD} is increased, the difference between core and tail QDs becomes less and less significant. At $w_{QD} = 2\gamma$ (bottom right panel of Fig. 8) the distinction between core and tail QDs has disappeared and the activation curve is fitted extremely well by a Lorentzian the width of which we can now consider as an experimentally measurable aspect of the physics of the nanolaser.

APPENDIX G: RELATION BETWEEN DETUNING, ACTIVATION CURVE WIDTH, AND QUANTUM-DOT DISPERSION

The dispersion of the quantum dots affects the frequency detuning of the lasing solution with respect to the cavity frequency $\Delta\omega$ and the width w_L of the activation curve, Eq. (1). To characterize this we have computed for each sample the average detuning $\overline{\Delta\nu}$ and its standard deviation, $\overline{w}$. Their values for each sample are reported in panels 1–10 of Fig. 9.

From this figure we can see that, as a general rule, the higher the sample detuning the higher the lasing frequency detuning. For example, samples 9, 8, and 10 have the three highest sample detunings $\overline{\Delta\nu}$, and their corresponding lasing solutions have the three highest detunings, $|\Delta\omega|$, in the same order. Conversely, the lasing solution of the sample with the smallest detuning, S_3, has the smallest detuning.

The width of the activation curve, w_L, depends on how compact the distribution of quantum dots is, in broadly the same way as discussed in Appendix F. As a general rule, samples with narrow distributions, i.e., small values of $\overline{w}$, have wide activation curves, e.g., samples S_4 and S_8, while samples with broad distributions have narrower activation curves, e.g., sample S_9. In samples with narrow distributions most quantum dots are active and there is more energy in the system. This filters down to the fixed number of quantum dots that we have set with higher detuning lifting their energy and broadening the activation curve. In samples with broader distributions, fewer quantum dots are maximally active and therefore the quantum dots in the tail have less energy, thus producing narrower activation curves.

APPENDIX H: ACTIVATION CURVES FOR CIM$^{(d)}$ AND TPM$^{(d)}_{1F}$

The influence of the width w_{QD} of the QD detuning distribution is further analyzed in Fig. 10 where we plot the amplitude a_L of the activation curve versus the frequency shift $|\Delta\omega|$ of the lasing solution with respect to the cavity frequency for the CIM$^{(d)}$ and TPM$^{(d)}_{1F}$ from left to right respectively. Each panel contains the outcome of the simulation of ten batches of $N = 50$ QDs sampled from distributions with widths $w_{QD} = [0.2, 0.5, 1.0, 2.0]\gamma$. The behavior is very similar to that of the TPM$^{(d)}$, but the points are less scattered due to a lower numerical noise in the estimation of the threshold.

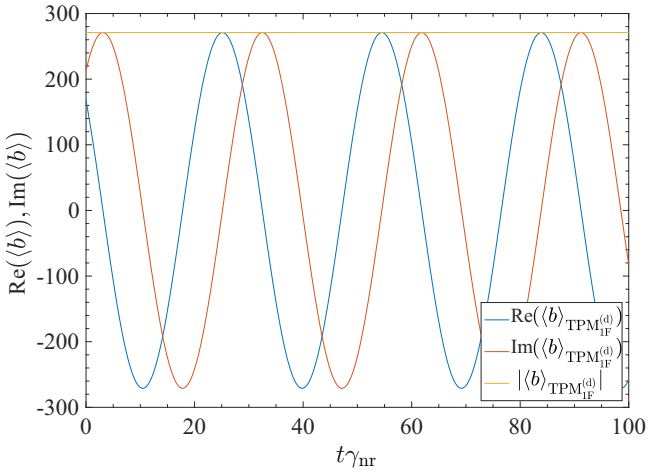

FIG. 11. Real and imaginary parts and modulus of the coherent field $\langle b\rangle$ computed using the TPM$_{1F}$ equations at pump $r = 2 \times 10^{14}$ s^{-1} for sample S_3. This is the rightmost point in the TPM$^{(d)}_{1F}$ curve in Fig. 3 in the main text and all parameter values are as in this figure.

APPENDIX I: SYNCHRONIZATION OF QDS AND EMERGENCE OF THE OSCILLATING COHERENT FIELD

Another effect of QD detuning is the emergence of single-frequency temporal oscillations in the coherent field (see Fig. 11), which is due to the synchronization of QDs with different resonant frequencies.

[1] A. L. Efros and M. Rosen, The electronic structure of semiconductor nanocrystals, Annu. Rev. Mater. Sci. **30**, 475 (2000).

[2] M. Lorke, F. Jahnke, and W. Chow, Excitation dependences of gain and carrier-induced refractive index change in quantum-dot lasers, Appl. Phys. Lett. **90**, 051112 (2007).

[3] H. Deng, G. L. Lippi, J. Mørk, J. Wiersig, and S. Reitzenstein, Physics and applications of high-β micro-and nanolasers, Adv. Opt. Mater. **9**, 2100415 (2021).

[4] D. Bimberg, Semiconductor nanostructures for flying q-bits and green photonics, Nanophotonics **7**, 1245 (2018).

[5] R. Soref, Tutorial: Integrated-photonic switching structures, Apl Photon. **3**, 021101 (2018).

[6] C.-Z. Ning, Semiconductor nanolasers and the size-energy-efficiency challenge: A review, Adv. Photon. **1**, 014002 (2019).

[7] J. R. Orchard, C. Woodhead, S. Shutts, J. Wu, A. Sobiesierski, R. J. Young, R. Beanland, H. Liu, P. M. Smowton, and D. J. Mowbray, Analysing radiative and non-radiative recombination in InAs QDs on Si for integrated laser applications, in *Quantum Dots and Nanostructures: Growth, Characterization, and Modeling XIII*, SPIE Proceedings Vol. 9758 (SPIE, Bellingham, WA, 2016), pp. 18–24.

[8] C. R. Fitch, A. Baltušis, I. P. Marko, D. Jung, J. C. Norman, J. E. Bowers, and S. J. Sweeney, Carrier recombination properties of low-threshold 1.3 μm quantum dot lasers on silicon, IEEE J. Sel. Top. Quantum Electron. **28**, 1 (2021).

[9] P. Michler, A. Kiraz, L. Zhang, C. Becher, E. Hu, and A. Imamoglu, Laser emission from quantum dots in microdisk structures, Appl. Phys. Lett. **77**, 184 (2000).

[10] V. I. Klimov, *Semiconductor and Metal Nanocrystals: Synthesis and Electronic and Optical Properties* (CRC, Boca Raton, FL, 2003).

[11] A. F. Phillips, S. J. Sweeney, A. R. Adams, and P. J. Thijs, The temperature dependence of 1.3 and 1.5 μm compressively strained inGaAs (P) MQW semiconductor lasers, IEEE J. Sel. Top. Quantum Electron. **5**, 401 (1999).

[12] N. Massé, I. Marko, A. Adams, and S. Sweeney, Temperature insensitive quantum dot lasers: Are we really there yet? J. Mater. Sci.: Mater. Electron. **20**, 272 (2009).

[13] Y. Arakawa and H. Sakaki, Multidimensional quantum well laser and temperature dependence of its threshold current, Appl. Phys. Lett. **40**, 939 (1982).

[14] Q. Gong, R. Nötzel, P. Van Veldhoven, T. Eijkemans, and J. Wolter, Wavelength tuning of InAs quantum dots grown on InP (100) by chemical-beam epitaxy, Appl. Phys. Lett. **84**, 275 (2004).

[15] S. Anantathanasarn, R. Nötzel, P. Van Veldhoven, F. Van Otten, Y. Barbarin, G. Servanton, T. de Vries, E. Smalbrugge, E. Geluk, T. Eijkemans *et al.*, Lasing of wavelength-tunable (1.55 μm region) InAs/InGa AsP/InP (100) quantum dots grown by metal organic vapor-phase epitaxy, Appl. Phys. Lett. **89**, 073115 (2006).

[16] S. E. White and M. A. Cataluna, Unlocking spectral versatility from broadly-tunable quantum-dot lasers, Photonics **2**, 719 (2015).

[17] S. Strauf and F. Jahnke, Single quantum dot nanolaser, Laser Photon. Rev. **5**, 607 (2011).

[18] K. J. Vahala, Optical microcavities, Nature (London) **424**, 839 (2003).

[19] L. Feng, R. El-Ganainy, and L. Ge, Non-Hermitian photonics based on parity–time symmetry, Nat. Photon. **11**, 752 (2017).

[20] K. Takata and M. Notomi, Photonic topological insulating phase induced solely by gain and loss, Phys. Rev. Lett. **121**, 213902 (2018).

[21] K. Takata, K. Nozaki, E. Kuramochi, S. Matsuo, K. Takeda, T. Fujii, S. Kita, A. Shinya, and M. Notomi, Observing exceptional point degeneracy of radiation with electrically pumped photonic crystal coupled-nanocavity lasers, Optica **8**, 184 (2021).

[22] F. Hentinger, M. Hedir, B. Garbin, M. Marconi, L. Ge, F. Raineri, J. A. Levenson, and A. M. Yacomotti, Direct observation of zero modes in a non-Hermitian optical nanocavity array, Photon. Res. **10**, 574 (2022).

[23] A. Fischer, T. V. Raziman, W. K. Ng, J. Clarysse, D. Saxena, J. Dranczewski, S. Vezzoli, H. Schmid, K. Moselund, and R. Sapienza, Controlling lasing around exceptional points in coupled nanolasers, npj Nanophoton. **1**, 6 (2024).

[24] C. B. Murray, C. R. Kagan, and M. G. Bawendi, Synthesis and characterization of monodisperse nanocrystals and close-packed nanocrystal assemblies, Annu. Rev. Mater. Sci. **30**, 545 (2000).

[25] W. Langbein, J. M. Hvam, M. Umlauff, H. Kalt, B. Jobst, and D. Hommel, Binding-energy distribution and dephasing of localized biexcitons, Phys. Rev. B **55**, R7383 (1997).

[26] W. Langbein, P. Borri, U. Woggon, V. Stavarache, D. Reuter, and A. D. Wieck, Radiatively limited dephasing in InAs quantum dots, Phys. Rev. B **70**, 033301 (2004).

[27] F. Jahnke, C. Gies, M. Aßmann, M. Bayer, H. Leymann, A. Foerster, J. Wiersig, C. Schneider, M. Kamp, and S. Höfling, Giant photon bunching, superradiant pulse emission and excitation trapping in quantum-dot nanolasers, Nat. Commun. **7**, 11540 (2016).

[28] J. Hendrickson, B. C. Richards, J. Sweet, S. Mosor, C. Christenson, D. Lam, G. Khitrova, H. M. Gibbs, T. Yoshie, A. Scherer, O. B. Shchekin, and D. G. Deppe, Quantum dot photonic-crystal-slab nanocavities: Quality factors and lasing, Phys. Rev. B **72**, 193303 (2005).

[29] A. P. Alivisatos, Semiconductor clusters, nanocrystals, and quantum dots, Science **271**, 933 (1996).

[30] V. I. Klimov, A. Mikhailovsky, S. Xu, A. Malko, J. A. Hollingsworth, A. C. Leatherdale, H.-J. Eisler, and M. Bawendi, Optical gain and stimulated emission in nanocrystal quantum dots, Science **290**, 314 (2000).

[31] M. Nirmal and L. Brus, Luminescence photophysics in semiconductor nanocrystals, Acc. Chem. Res. **32**, 407 (1999).

[32] P. Reiss, M. Protiere, and L. Li, Core/shell semiconductor nanocrystals, Small **5**, 154 (2009).

[33] Z. Yang, M. Pelton, I. Fedin, D. V. Talapin, and E. Waks, A room temperature continuous-wave nanolaser using colloidal quantum wells, Nat. Commun. **8**, 143 (2017).

[34] M. Grundmann, The present status of quantum dot lasers, Physica E **5**, 167 (1999).

[35] M. Sugawara, K. Mukai, Y. Nakata, H. Ishikawa, and A. Sakamoto, Effect of homogeneous broadening of optical gain on lasing spectra in self-assembled $In_xGa_{1-x}As/GaAs$ quantum dot lasers, Phys. Rev. B **61**, 7595 (2000).

[36] M. Sugawara, N. Hatori, H. Ebe, M. Ishida, Y. Arakawa, T. Akiyama, K. Otsubo, and Y. Nakata, Modeling room-temperature lasing spectra of 1.3 μm self-assembled InAs/GaAs quantum-dot lasers: Homogeneous broadening of optical gain under current injection, J. Appl. Phys. **97**, 043523 (2005).

[37] K. M. Cha, I. Horiuchi, K. Shibata, and K. Hirakawa, Size-limiting effect of site-controlled InAs quantum dots grown at high temperatures by molecular beam epitaxy, Appl. Phys. Express **5**, 085501 (2012).

[38] H. Lan and Y. Ding, Ordering, positioning and uniformity of quantum dot arrays, Nano Today **7**, 94 (2012).

[39] M. Felici, P. Gallo, A. Mohan, B. Dwir, A. Rudra, and E. Kapon, Site-controlled inGaAs quantum dots with tunable emission energy, Small **5**, 938 (2009).

[40] C. Schneider, S. Höfling, and M. Kamp, In(Ga)As/GaAs site-controlled quantum dots with tailored morphology and high optical quality, Phys. Status Solidi A **209**, 2379 (2012).

[41] A. Kaganskiy, F. Gericke, T. Heuser, T. Heindel, X. Porte, and S. Reitzenstein, Micropillars with a controlled number of site-controlled quantum dots, Appl. Phys. Lett. **112**, 071101 (2018).

[42] J. Große, M. von Helversen, A. Koulas-Simos, M. Hermann, and S. Reitzenstein, Development of site-controlled quantum dot arrays acting as scalable sources of indistinguishable photons, APL Photon. **5**, 096107 (2020).

[43] X. Zhao, W. Liu, Y. Bao, X. Chen, C. Ji, G. Yang, B. Wei, F. Yang, and X. Wang, Site-controlled growth of In(Ga)As/GaAs quantum dots on patterned substrate, Nanotechnology **36**, 052001 (2025).

[44] M. Podhorský, M. Klonz, I. Limame, S. Tripathi, K. Gaur, C. C. Palekar, P. Mudi, P. Klenovský, S. Rodt, and S. Reitzenstein, Site-controlled growth of inGaAs quantum dots based on buried stressors for the development of microlasers and quantum light sources, J. Phys.: Conf. Ser. **2931**, 012016 (2024).

[45] C.-W. Shih, I. Limame, C. C. Palekar, A. Koulas-Simos, A. Kaganskiy, P. Klenovský, and S. Reitzenstein, Self-aligned photonic defect microcavity lasers with site-controlled quantum dots, Laser Photon. Rev. **18**, 2301242 (2024).

[46] V. Khatri, V. Sichkovskyi, L. Popilevsky, Y. Kauffmann, G. Eisenstein, and J. P. Reithmaier, Increased modal gain in 1.55 μm quantum dot lasers based on improved size

homogeneity obtained by comprehensive growth optimization, ACS Photon. **12**, 3687 (2025).

[47] C. Shen, W. Zhan, K. Xin, M. Li, Z. Sun, H. Cong, C. Xu, J. Tang, Z. Wu, B. Xu *et al.*, Machine-learning-assisted and real-time-feedback-controlled growth of InAs/GaAs quantum dots, Nat. Commun. **15**, 2724 (2024).

[48] A. Kaganskiy, S. Kreinberg, X. Porte, and S. Reitzenstein, Micropillar lasers with site-controlled quantum dots as active medium, Optica **6**, 404 (2019).

[49] A. Abdollahinia, S. Banyoudeh, A. Rippien, F. Schnabel, O. Eyal, I. Cestier, I. Kalifa, E. Mentovich, G. Eisenstein, and J. Reithmaier, Temperature stability of static and dynamic properties of 1.55 μm quantum dot lasers, Opt. Express **26**, 6056 (2018).

[50] M. Bayer, F. Weidner, A. Larionov, A. McDonald, A. Forchel, and T. L. Reinecke, Inhibition and enhancement of the spontaneous emission of quantum dots in structured microresonators, Phys. Rev. Lett. **86**, 3168 (2001).

[51] M. Lodde, R. P. van Veldhoven, E. Verhagen, and A. Fiore, The effect of In(Ga)As/GaAs quantum dots on the optical loss of photonic crystal cavities, J. Appl. Phys. **135**, 063103 (2024).

[52] P. Harrison and A. Valavanis, *Quantum Wells, Wires and Dots: Theoretical and Computational Physics of Semiconductor Nanostructures* (Wiley, New York, 2016).

[53] S. Sapra and D. D. Sarma, Evolution of the electronic structure with size in II-VI semiconductor nanocrystals, Phys. Rev. B **69**, 125304 (2004).

[54] I. E. Protsenko and A. V. Uskov, Perturbation approach in Heisenberg equations for lasers, Phys. Rev. A **105**, 053713 (2022).

[55] A. M. Yacomotti, Z. Denis, A. Biella, and C. Ciuti, Quantum density matrix theory for a laser without adiabatic elimination of the population inversion: Transition to lasing in the class-b limit, Laser Photon. Rev. **17**, 2200377 (2023).

[56] A. A. Vyshnevyy, Gain-dependent Purcell enhancement, breakdown of Einstein's relations, and superradiance in nanolasers, Phys. Rev. B **105**, 085116 (2022).

[57] J. Fricke, Transport equations including many-particle correlations for an arbitrary quantum system: A general formalism, Ann. Phys. (NY) **252**, 479 (1996).

[58] W. Chow and F. Jahnke, On the physics of semiconductor quantum dots for applications in lasers and quantum optics, Prog. Quantum Electron. **37**, 109 (2013).

[59] W. Chow, F. Jahnke, and C. Gies, Emission properties of nanolasers during the transition to lasing, Light Sci. Appl. **3**, e201 (2014).

[60] S. Kreinberg, W. W. Chow, J. Wolters, C. Schneider, C. Gies, F. Jahnke, S. Höfling, M. Kamp, and S. Reitzenstein, Emission from quantum-dot high-ß microcavities: Transition from spontaneous emission to lasing and the effects of superradiant emitter coupling, Light Sci. Appl. **6**, e17030 (2017).

[61] C. Gies, J. Wiersig, M. Lorke, and F. Jahnke, Semiconductor model for quantum-dot-based microcavity lasers, Phys. Rev. A **75**, 013803 (2007).

[62] M. A. Carroll, G. D'Alessandro, G. L. Lippi, G.-L. Oppo, and F. Papoff, Thermal, quantum antibunching and lasing thresholds from single emitters to macroscopic devices, Phys. Rev. Lett. **126**, 063902 (2021).

[63] M. Carroll, G. D'Alessandro, G. Lippi, G.-L. Oppo, and F. Papoff, Photon-number squeezing in nano- and microlasers, Appl. Phys. Lett. **119**, 101102 (2021).

[64] J.-S. Tempel, I. Akimov, M. Aßmann, C. Schneider, S. Höfling, C. Kistner, S. Reitzenstein, L. Worschech, A. Forchel, and M. Bayer, Extrapolation of the intensity autocorrelation function of a quantum-dot micropillar laser into the thermal emission regime, J. Opt. Soc. Am. B **28**, 1404 (2011).

[65] M. A. Carroll, G. D'Alessandro, G. L. Lippi, G.-L. Oppo, and F. Papoff, Coherence buildup and laser thresholds from nanolasers to macroscopic lasers, Phys. Rev. A **107**, 063710 (2023).

[66] F. Papoff, M. A. Carroll, G. L. Lippi, G.-L. Oppo, and G. D'Alessandro, Quantum correlations, mixed states, and bistability at the onset of lasing, Phys. Rev. A **111**, L011501 (2025).

[67] M. A. Carroll, G. D'Alessandro, G. L. Lippi, G.-L. Oppo, and F. Papoff, Carroll reply: Thermal, quantum antibunching and lasing thresholds from single emitters to macroscopic devices, Phys. Rev. Lett. **128**, 029402 (2022).

[68] N. Baer, C. Gies, J. Wiersig, and F. Jahnke, Luminescence of a semiconductor quantum dot system, Eur. Phys. J. B **50**, 411 (2006).

[69] M. Kira and S.W. Koch, *Semiconductor Quantum Optics* (Cambridge University, New York, 2011).

[70] M. Florian, C. Gies, F. Jahnke, H. A. M. Leymann, and J. Wiersig, Equation-of-motion technique for finite-size quantum-dot systems: Cluster expansion method, Phys. Rev. B **87**, 165306 (2013).

[71] M. Schwab, H. Kurtze, T. Auer, T. Berstermann, M. Bayer, J. Wiersig, N. Baer, C. Gies, F. Jahnke, J. P. Reithmaier, A. Forchel, M. Benyoucef, and P. Michler, Radiative emission dynamics of quantum dots in a single cavity micropillar, Phys. Rev. B **74**, 045323 (2006).

[72] M. Saldutti, Y. Yu, and J. Mørk, The onset of lasing in semiconductor nanolasers, Laser Photon. Rev. **18**, 2300840 (2024).

[73] G. D'Alessandro, G.L. Lippi, and F. Papoff, QD lasers GitHub site, https://github.com/giampaolo314/QD_laser_models.